Overhauser enhanced magnetic resonance imaging for tumor oximetry: Coregistration of tumor anatomy and tissue oxygen concentration

Murali C. Krishna[†‡], Sean English[†], Kenichi Yamada[†], John Yoo[†], Ramachandran Murugesan[†], Nallathamby Devasahayam[†], John A. Cook[†], Klaes Golman[§], Jan Henrik Ardenkjaer-Larsen[§], Sankaran Subramanian[†], and James B. Mitchell[†]

[†]Radiation Biology Branch, Center for Cancer Research, National Cancer Institute, National Institutes of Health, Bethesda, MD 20892; and [§]Nycomed Innovation AB, MEDEON, SE-205 12 Malmo, Sweden

Communicated by Albert W. Overhauser, Purdue University, West Lafayette, IN, December 14, 2001 (received for review October 19, 2001)

An efficient noninvasive method for *in vivo* imaging of tumor oxygenation by using a low-field magnetic resonance scanner and a paramagnetic contrast agent is described. The methodology is based on Overhauser enhanced magnetic resonance imaging (OMRI), a functional imaging technique. OMRI experiments were performed on tumor-bearing mice (squamous cell carcinoma) by i.v. administration of the contrast agent Oxo63 (a highly derivatized triarylmethyl radical) at nontoxic doses in the range of 2–7 mmol/kg either as a bolus or as a continuous infusion. Spatially resolved pO_2 (oxygen concentration) images from OMRI experiments of tumor-bearing mice exhibited heterogeneous oxygenation profiles and revealed regions of hypoxia in tumors (<10 mmHg; 1 mmHg = 133 Pa). Oxygenation of tumors was enhanced on carbogen (95% O_2/5% CO_2) inhalation. The pO_2 measurements from OMRI were found to be in agreement with those obtained by independent polarographic measurements using a pO_2 Eppendorf electrode. This work illustrates that anatomically coregistered pO_2 maps of tumors can be readily obtained by combining the good anatomical resolution of water proton-based MRI, and the superior pO_2 sensitivity of EPR. OMRI affords the opportunity to perform noninvasive and repeated pO_2 measurements of the same animal with useful spatial (≈1 mm) and temporal (2 min) resolution, making this method a powerful imaging modality for small animal research to understand tumor physiology and potentially for human applications.

Abnormal values of pO_2 (the partial pressure of O_2) are linked to many pathophysiological conditions (e.g., ischemic diseases, reperfusion injury, and oxygen toxicity). Approximately one-third of human tumors evaluated for oxygen status have shown significant oxygen deficiency, and oxygen deficiency increases the tumor's resistance toward cancer treatment modalities, including radiation and chemotherapy (1, 2). Additionally, hypoxic microenvironments in tumors are known to promote processes driving malignant progression, such as angiogenesis, elimination of p53 tumor suppressor activity, genetic instability, and metastasis (3–5). Understanding of tumor hypoxia could lead to the discovery of diagnostic and prognostic markers for malignant progression, discovery of novel therapeutic targets, and the development of new constructs for gene therapy applications in human cancer. Hence, a noninvasive technique that could accurately and repetitively measure tissue oxygenation would find broad application in clinical and basic research. Unfortunately, the currently used electrochemical method (6) for *in vivo* oxygen measurement is an invasive technique applicable only to accessible tumors. Further, the technique is hampered by measurements of only a small part of the total tumor, which cannot be re-evaluated. Several magnetic resonance techniques (7, 8) have been developed for *in vivo* oximetry, including spin label oximetry (9), MRI (10), and electron paramagnetic resonance imaging (EPRI) (11, 12). The blood oxygen level-dependent effect, mainly used for functional MRI, has more recently found application in evaluating efficacy of oxygenation by certain oxygenating modalities in hypoxic tumors, but it does not provide quantitative oximetry (13). Direct NMR measurements of the proximal histidine of myoglobin or hemoglobin show much less sensitivity than the water proton based experiments (14). ^{19}F MRI of blood substitutes is also used for oximetry, but suffers from chemical shift artifacts and low ^{19}F concentration in tissues (15).

EPR methods (both spectroscopic and imaging) show better sensitivity to oxygen concentration than the NMR methods (9, 11). In EPRI, the spatial as well as the spectral information of the exogenously administered spin probes is obtained. Hence, EPR images present the *in vivo* visualization of the spin probes often without complementary anatomical information. In contrast, MRI is a well-established modality that gives superior anatomical information. Overhauser MRI (OMRI) is a double resonance technique (16, 17) that couples the advantages of MRI with the sensitivity of EPR, by making use of the Overhauser effect (18). By saturating the EPR transition of a paramagnetic agent, the NMR signal intensities of the coupled water protons are enhanced by a significant factor by means of the Overhauser effect. The Overhauser enhancement (OE) depends on the line width of the paramagnetic agent, which in turn depends on oxygen concentration (9, 11), making it possible for coregistration of both the anatomical structures and the corresponding oxygen status. With the recent availability of biologically compatible paramagnetic spin probes based on the triaryl methyl structure (19, 20), *in vivo* OMRI was applied toward determining the tissue oxygen status of small animals. In the present study, we used a narrow-line trityl-based contrast agent to demonstrate the feasibility of obtaining morphological images of high resolution, coregistered with oxygen concentration information. Based on these images, the pO_2 status of any specific location in the tumor can be interrogated accurately and repeatedly, thus providing a useful approach to evaluate the importance of oxygen status in tumor physiology.

Materials and Methods

OMRI Scanner. The OMRI experiments were performed at the National Cancer Institute on a custom-built (Philips Research Laboratories, Hamburg) human whole-body magnet (79 cm diameter; 125 cm length) operating in a field-cycled mode to avoid excess power deposition during the EPR cycle. The EPR B_0 is at 8.1 mT, and the NMR B_0 is 15 mT. Although the NMR

Abbreviations: MR, magnetic resonance; OMRI, Overhauser enhanced MRI; EPR, electron paramagnetic resonance; OE, Overhauser enhancement; SNR, signal-to-noise ratio; SCC, squamous cell carcinoma; RF, radiofrequency.

[‡]To whom reprint requests should be addressed. E-mail: murali@helix.nih.gov.

The publication costs of this article were defrayed in part by page charge payment. This article must therefore be hereby marked "*advertisement*" in accordance with 18 U.S.C. §1734 solely to indicate this fact.

2216–2221 | PNAS | February 19, 2002 | vol. 99 | no. 4 www.pnas.org/cgi/doi/10.1073/pnas.042671399

B_0 can be ramped to higher values, the current power supply capabilities do not permit values of more than 15 mT. The resonator assembly to study mice was tuned to 625 kHz and consists of the NMR transmit saddle coil (25 cm diameter, 23 cm length) and a solenoidal receive coil (3 cm i.d., 60 mm length) with a bandwidth of 80 kHz. The maximum transmit power is 250 W (peak). For EPR, a saddle coil (13. 5 cm diameter, 23.5 cm length) tuned to 226 MHz and concentric to the NMR coils is used. The maximum transmit power was 100 W, and the efficiency parameter of the EPR coil used was measured to be 5.2 $\mu T/W^{1/2}$.

Contrast Agent. The chemical structure of the contrast agent Oxo63 is given in Fig. 1*A*. It is based on a triarylmethyl (trityl radical) structure, which is derivatized extensively to confer optimal chemical, pharmacological, and EPR characteristics (such as stability, water-solubility, low toxicity, long *in vivo* half-lives, single narrow-line resonance, and pO_2-dependent EPR line widths) (20). The molecular weight of Oxo63 is 1,427 and its intrinsic line width (a_3) is 4.0 μT. The oxygen-dependent line width (a_1) was estimated to be 57 μT/mM O_2, and the concentration-dependent self-broadening (a_2) is 0.2 μT/mM Oxo63. The relaxivity of Oxo63 in blood is 0.3 $mM^{-1} \cdot s^{-1}$. The Oxo63 solutions were freshly prepared by dissolving the dry powder in sterile PBS prior to i.v. injection. The concentration of Oxo63 was calculated by using its absorbance at 464 nm ($\varepsilon_{464} = 17\ mM^{-1} \cdot cm^{-1}$), and doses between 2.0 and 7.0 mmol/kg were administered by i.v. injection. The concentration of solution for injection was usually maintained at 200 mM, and the agent was given either as a bolus or as a continuous infusion (11 μl/min). The LD_{50} of Oxo63 in mice is 8 mmol/kg and the maximally tolerated dose is in the range of 2.5–7.0 mmol/kg. The pharmacologic half-life of Oxo63 in the kidney and blood was ≈12 min, whereas in the tumor, the values were at least twice as long.

Pulse Sequence. OMRI experiments were performed by using standard spin warp gradient echo sequence for MRI, where each phase encoding step was preceded by an EPR saturation pulse to elicit the OE (Fig. 1*B*). The EPR pulse width at a given power was typically in the range of 200–300 ms, in the order of the proton T_1. The pulse sequence started with the ramping of the B_0 field to 8.1 mT, corresponding to the EPR irradiation. It was followed by switching on the EPR irradiation (226 MHz) for a period of about 200 ms. Then the B_0 field was ramped to 15 mT before the radiofrequency (RF) pulse and the associated field gradients are turned on. For pO_2 imaging, OMRI images were collected with interleaving pulse sequences in which the EPR irradiation was applied at two different power levels corresponding to high-power (45 W) and low-power (3 W) images, before each phase-encoding gradient. Also, at the beginning or end of the cycle, a conventional MRI (without EPR on) was collected for computing the enhancement factors. A Hewlett Packard PC (operating system, LINUX 5.2) was used for data acquisition. The images were reconstructed from the echoes by using standard software implemented in the system and were stored in DICOM format (Digital Imaging and Communications in Medicine). Further image processing, such as segmentation, histogram equalization, and quantitative parameter calculation, was done by using programs coded in MATLAB. Typical scan conditions in OMRI are $T_{EPR}/T_R/T_E$ = 300 ms/450 ms/25 ms; no. of averages = 1; 128 phase-encoding steps. The pixel size was 0.63 mm × 0.63 mm with a slice thickness of 5 mm. The image field of view 80 mm was represented by a 128 × 128 size matrix.

Animal Studies. Female C3H mice produced by the National Cancer Institute Animal Production Area (Frederick, MD) were used for the study. The mice were 6–8 weeks of age at the time of experiment and weighed between 20 and 30 g. OMRI experiments were carried out in compliance with the *Guide for the Care and Use Of Laboratory Animal Resources*, (*1996*) National Research Council, and approved by the National Cancer Institute

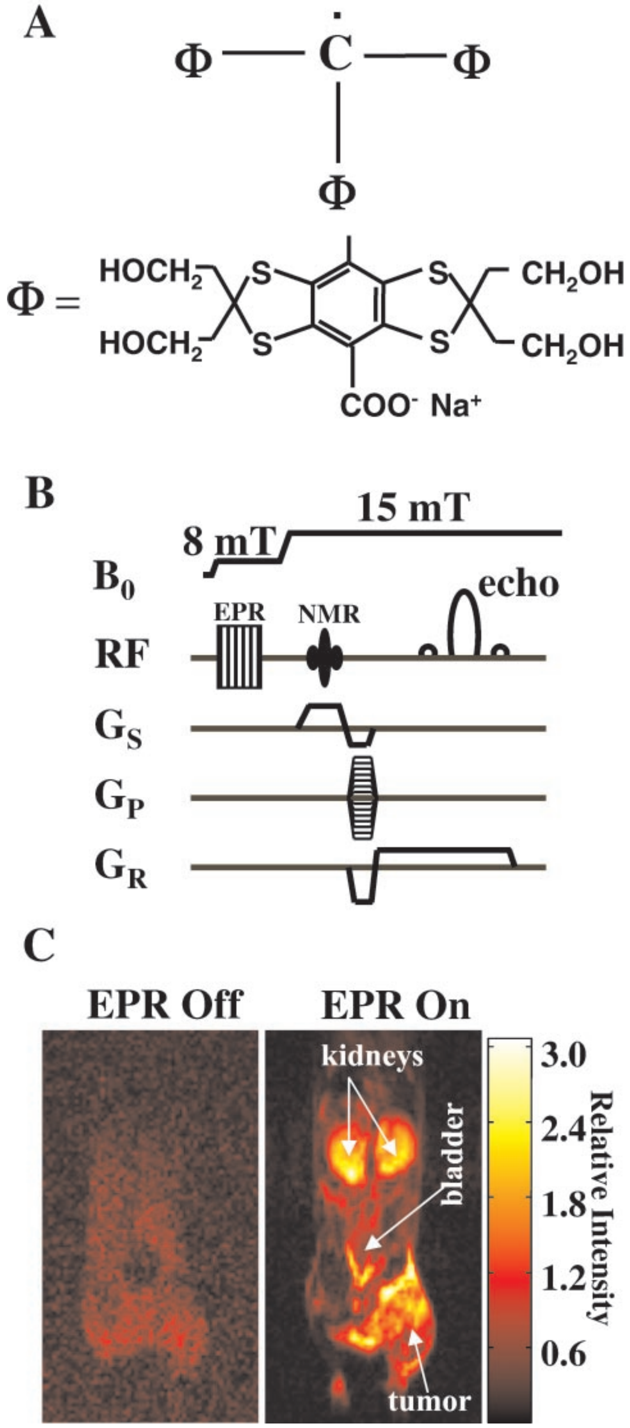

Fig. 1. (*A*) Structural formula of the contrast agent Oxo63, tris[8-carboxy-2,2,6,6-tetrakis(2-hydroxymethyl)benzo[1,2-*d*:4,5-*d*′]bis(1,3)dithio-4-yl]methyl radical, trisodium salt. (*B*) OMRI pulse-sequence diagram showing B_0 field cycling and radiofrequency (RF) and field-gradient waveforms. (*C*) Interleaved (''EPR off'' and ''EPR on'') OMRI images (coronal) of a female C3H mouse, bearing SCC tumor on the right hind leg, demonstrating the Overhauser enhancement (OE) and the diagnostic quality achievable at this low magnetic field of 15 mT. The mouse was administered 3.8 mmol/kg Oxo63 by tail vein cannulation. Both images were acquired in the presence of the contrast agent. The image acquisition parameters are given in *Materials and Methods*.

Animal Care and Use Committee. Tumors were grown in the mice by an intramuscular (s.c.) injection of a single-cell suspension of 10^6 squamous cell carcinoma (SCC) cells on the right hind leg. The tumors grew to a size of 1.0-cm diameter ($\approx$500 mm^3) in approximately 8 days, and tumors of this size were used for all imaging and oxygen electrode studies (detailed below). For imaging experiments, the tail vein was cannulated with a catheter before induction of anesthesia. Before Oxo63 infusion, a bolus of gadolinium diethylenetriaminopentaacetic acid (150 μl of 100 mM) was introduced in the bladder (urinary tract catheterization) to minimize the strong image intensity from the bladder (predominantly by reducing the leakage factor *f*; see Eq. **1** below) resulting from accumulation of Oxo63 with time. Mice were anesthetized for imaging experiments by allowing them to breathe gas mixtures containing 1.5% isoflurane and air or carbogen (95% O_2/5% CO_2).

The mouse was placed in the resonator in a prone position such that the head was lying outside the resonator and breathing the anesthetic and air or carbogen. The active region of the resonator spanned the thoracic region to lower extremity. An appropriate slice was selected after the spin probe administration, by examining the projections for maximal intensities in the kidneys and tumor. The mice were killed by cervical dislocation after the completion of scans.

Polarographic pO_2 Measurements. Approximately the same experimental conditions used for OMRI were used for pO_2 measurements by the Eppendorf electrode. Mice were allowed to continuously breathe isoflurane/air for 15 min while pO_2 measurements were taken with an Eppendorf probe. Two tracks parallel and two tracks perpendicular to the femur (total of $\approx$55 individual readings) were used to determine the median oxygen tension in each tumor. Isoflurane/carbogen was then continuously administered for 15 min while pO_2 measurements were taken in the same manner.

Computation of pO_2. Since its discovery in metals by Overhauser (18), many applications of dynamic nuclear polarization have been described (17, 21–23). Applications of OMRI to free radical imaging and oximetry have been recognized (24, 25). Nevertheless, a brief account of pO_2 computation from the OMRI images, pertaining to the work presented here, is outlined below.

When a paramagnetic contrast agent is irradiated by electromagnetic radiation, at resonance, the electron spin polarization is transferred to the proton because of the Overhauser effect. The OE, which is the amplitude of the enhanced proton magnetization, M^{I}, relative to thermal equilibrium, M_0^{I} is given by

$$\mathrm{OE} = [(M^{\mathrm{I}} - M_0^{\mathrm{I}})/M_0^{\mathrm{I}}] = (\gamma_{\mathrm{e}}/\gamma_{\mathrm{p}})fkS. \qquad [1]$$

Here *f* is the leakage factor; *k* is the coupling factor; *S* is the degree of saturation of the electron spin resonance; and $\gamma_{\mathrm{e}} = 658\ \gamma_{\mathrm{p}}$, where γ_{e} and γ_{p} are the magnetogyric factors of an unpaired electron and a proton, respectively. The coupling factor depends on the nature of interaction between the contrast agent and the protons and for purely dipolar interaction, $k = 0.5$. The leakage factor can be approximated to

$$f = rcT_{10}/(1 + rcT_{10}) = (R_1 - R_{10})/R_1, \qquad [2]$$

where T_{10} and T_1 are the relaxation times, and R_{10} and R_1, the corresponding relaxation rates, of the protons in the absence and presence of the contrast agent, and *r* and *c* are the relaxivity and concentration of the contrast agent, respectively. Up to a concentration of 5 mM, the value of $rcT_{10} \ll 1$, and hence $f = rcT_{10}$ (or rc/R_{10}). Modeling the line shape as Lorentzian, the degree of saturation, *S*, of the contrast agent may be written as:

$$S = (M_0^{\mathrm{S}} - M^{\mathrm{S}})/M_{\mathrm{o}}^{\mathrm{S}} = (\gamma_{\mathrm{e}}^2 B_{1\mathrm{e}}^2 T_{1\mathrm{e}} T_{2\mathrm{e}})/(1 + (\gamma_{\mathrm{e}}^2 B_{1\mathrm{e}}^2 T_{1\mathrm{e}} T_{2\mathrm{e}})), \qquad [3]$$

where $B_{1\mathrm{e}}$ is the EPR irradiation field and $T_{1\mathrm{e}}$ and $T_{2\mathrm{e}}$ are the electron spin relaxation times, which are mainly determined by the concentration of the contrast reagent and the oxygen-induced line broadening. In the concentration and pO_2 range of interest for *in vivo* studies, the effect of oxygen concentration (C_{O2}) and contrast reagent concentration (C_{CR}) on the relaxation rate can be expressed as

$$1/[\gamma_{\mathrm{e}}(T_{1\mathrm{e}}T_{2\mathrm{e}})^{1/2}] = a_1 C_{\mathrm{O2}} + a_2 C_{\mathrm{CR}} + a_3, \qquad [4]$$

where a_3 is the line width of the paramagnetic species at infinite dilution and in the absence of oxygen, and a_1 and a_2 are spectroscopic constants involving the oxygen-dependent and concentration-dependent line widths, respectively. The transient water proton magnetization measured in a double-resonance experiment is given by

$$M^{\mathrm{I}} = M_0^{\mathrm{I}} - E_{\mathrm{inf}} M_0^{\mathrm{I}}[1 - \exp(-T_{\mathrm{EPR}}/T_1)]f[\gamma_{\mathrm{e}}^2 B_{1\mathrm{e}}^2 T_{1\mathrm{e}} T_{2\mathrm{e}}/ (1 + \gamma_{\mathrm{e}}^2 B_{1\mathrm{e}}^2 T_{1\mathrm{e}} T_{2\mathrm{e}})], \qquad [5]$$

where T_{EPR} is the EPR irradiation time and E_{inf} is the enhancement factor at infinite EPR RF power and infinite concentration of the paramagnetic contrast agent. Eq. **5** gives the pixel intensity of the OMRI image. Thus from Eqs. **4** and **5** it can be seen that the enhancement factor depends on the concentration and line width of the contrast agent, on the strength of the EPR RF irradiation field, and on pO_2. If OMRI images are obtained at two different EPR power levels, B_{a} and B_{b}, then C_{CR} and C_{O2} can be estimated from

$$C_{\mathrm{CR}} = \{1/(E_{\mathrm{inf}} r T_{10})\}[(B_{\mathrm{a}}^2 - B_{\mathrm{b}}^2) I_{\mathrm{a}} I_{\mathrm{b}}/(B_{\mathrm{a}}^2 I_{\mathrm{b}} - B_{\mathrm{b}}^2 I_{\mathrm{a}})] \qquad [6]$$

and

$$C_{\mathrm{O2}} = (1/a_1)\{[B_{\mathrm{a}}^2 B_{\mathrm{b}}^2 (I_a - I_{\mathrm{b}})/(B_{\mathrm{a}}^2 \mathrm{I}_{\mathrm{b}} - B_{\mathrm{b}}^2 I_{\mathrm{a}})]^{1/2} - a_2 C_{\mathrm{CR}} - a_3\}, \qquad [7]$$

where $E_{\mathrm{inf}}^* = E_{\mathrm{inf}}[1 - \exp(-T_{\mathrm{EPR}}/T_{1\mathrm{e}})]$ and I_{a} and I_{b} are the pixel intensities of the two images normalized with respect to the native NMR image. Based on these principles, a computer program was written in C language to calculate the pO_2 and the contrast agent concentration.

Results

Fig. 1*C* shows a morphological image collected from an anesthetized mouse after i.v. infusion with Oxo63 (3.8 mmol/kg). The mouse had a 1-cm diameter tumor (SCC) on the right hind leg and was placed in the resonator assembly. A coronal slice with a thickness of 5 mm was selected for imaging. The image on the *Left*, which was collected in the absence of EPR irradiation and in the presence of the paramagnetic contrast agent, is characteristic of a magnetic resonance (MR) image with poor signal-to-noise ratio (SNR). The poor SNR and spatial resolution of the image are consistent with the low magnetic field (15 mT) at which the MR images were collected. Although the gross features of the mouse could be recognized, the image resolution is not sufficient to provide anatomical detail of the internal structures in the mouse. The image obtained when the MR images were collected after a period of EPR irradiation is shown in Fig. 1*C Right*. The image obtained under these conditions has significantly enhanced intensity. The in-plane resolution ($\approx$0.7 mm) in the image was sufficient to map internal structures. From the image, the two kidneys, bladder, and the tumor region could be readily recognized. From experiments conducted in more than 25 mice, it was observed that the SNR of the pixel intensities from these regions were consistently high (>20). The levels of Oxo63 were measured directly by EPR in several tissues such as liver, muscle, heart, kidneys, and tumor extracted after the animal was killed (data not shown). It was found

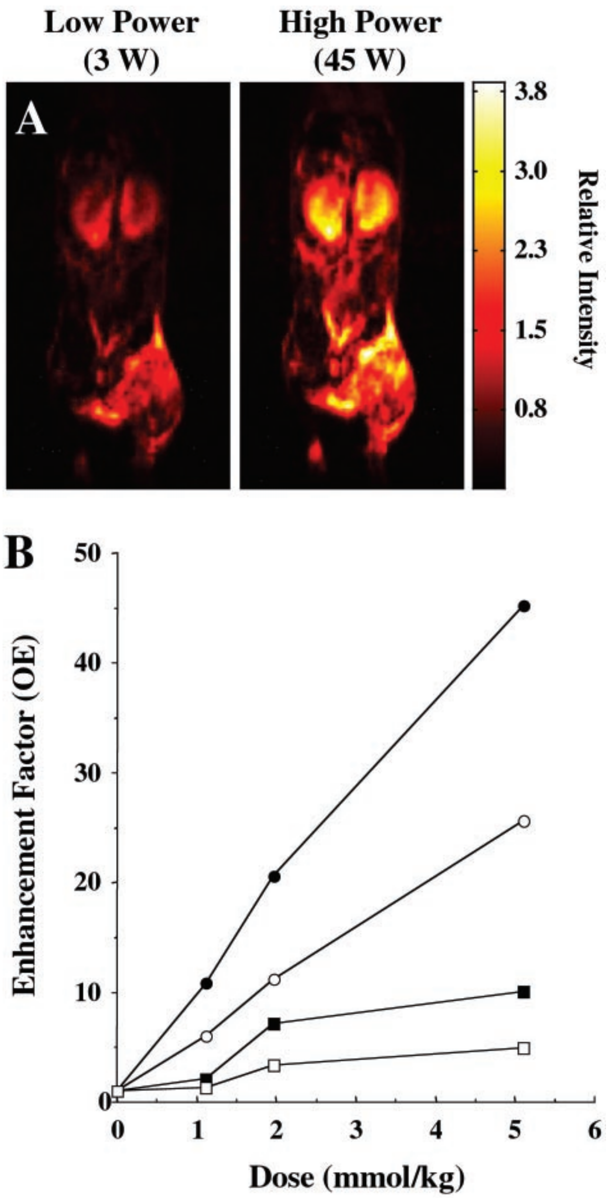

Fig. 2. (*A*) OMRI images taken at two different saturating EPR power levels. Image acquisition parameters are the same as given for Fig. 1. The SNR difference between these two images is 11, which enables reliable estimate of pO_2 maps (Fig. 3) by using the algorithm described in the experimental section. (*B*) The enhancement factors as a function of Oxo63 dose, calculated for kidney (●, high power; ■, low power) and tumor (○, high power; □, low power). The enhancement factors were calculated as the ratio of mean pixel value of a region of interest in the Overhauser image to the mean of the same region of interest for the conventional MR image (EPR off).

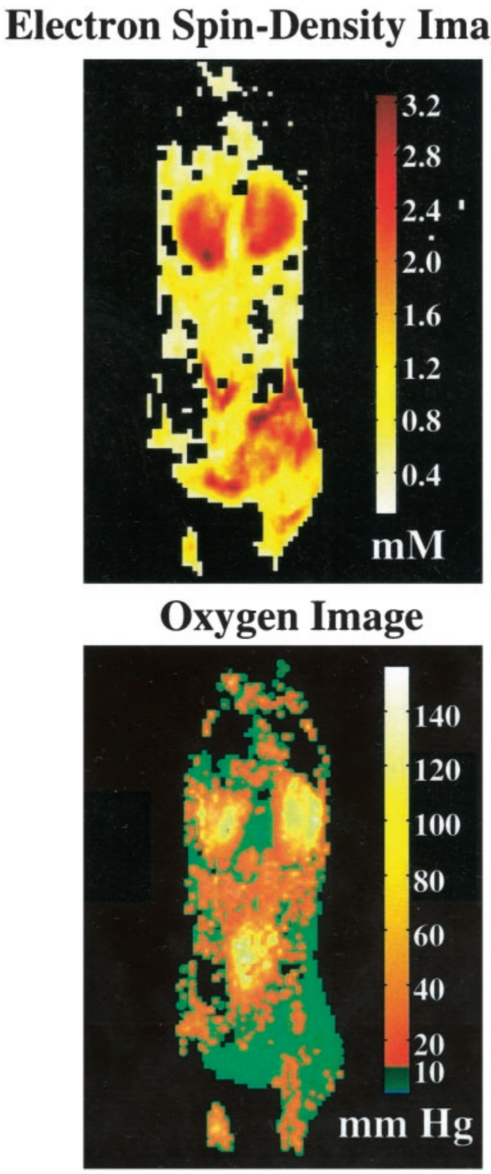

Fig. 3. Contrast agent and oxygen distribution maps of tumor-bearing female C3H mouse computed from OMRI images taken at two different power levels. The contrast in the spin-density image shows the differential accumulation of the spin probe, Oxo63. Nevertheless, the distribution is sufficient in many regions of interest to give an SNR above 10. The oxygen map indicates a relatively homogeneous pO_2 in kidney in contrast to significant heterogeneity in tumor. (1 mmHg = 133 Pa.)

that the enhancement of Oxo63 in kidneys, tumor, and bladder regions were consistently higher than that noted in muscle, liver, and lungs.

To a first approximation, the OE in a given pixel can depend mainly on four factors, namely (*i*) the strength of the EPR irradiation, (*ii*) the concentration of the paramagnetic spin probe, (*iii*) the proton T_1 in the tissue in the absence of the spin probe, and (*iv*) the pO_2 in the tissue. Because the mouse was uniformly exposed to EPR irradiation, the latter three conditions may account for different OE factors. Experimentally, OE factor, which depends on the strength of EPR irradiation, can be changed in a straightforward manner. However, in tissues where the T_1 of protons is inherently small ($<$200 ms), the experimentally realized OE might be less than in tissues with long T_1.

Fig. 2*A* shows anatomic images collected from a tumor-bearing mouse infused with Oxo63, by irradiating at two different EPR power levels (3 W and 45 W). The mouse was irradiated at these two power levels in an alternating manner. In agreement with Eq. **1**, when all other conditions were experimentally maintained, the image intensity increased with the strength of EPR irradiation. The dependence of OE in kidney and tumor on the dose of the contrast agent was plotted from the experimental data collected from several OMRI experiments in which tumor-bearing mice were given i.v. infusion of Oxo63 at different doses (Fig. 2*B*). As can be seen, the OE in a given tissue is directly dependent on the concentration of the paramagnetic agent. The SNR of the pixel intensities in both the tumor and kidneys was

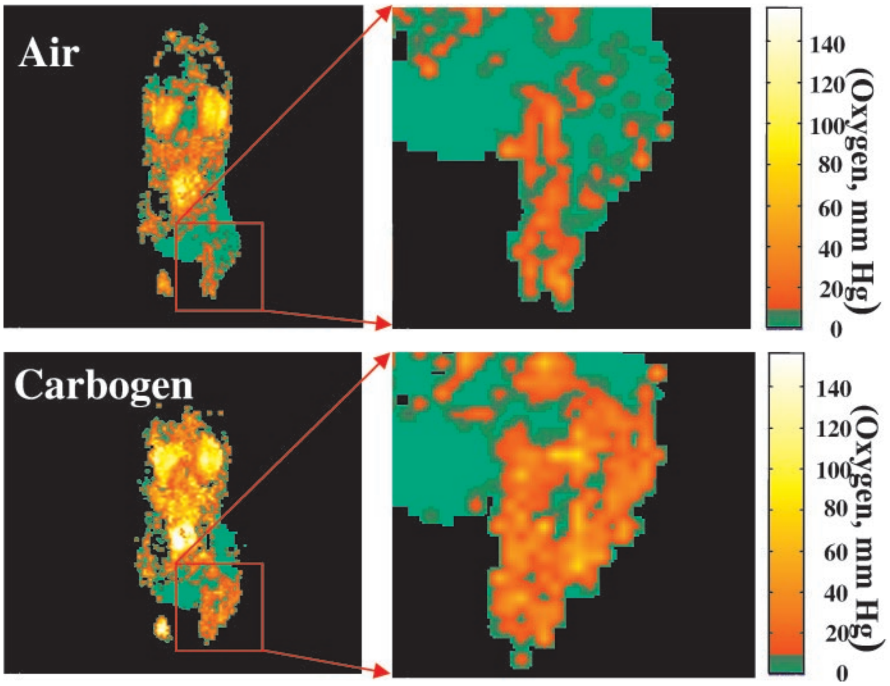

Fig. 4. pO_2 images a C3H mouse with a 1-cm diameter SCC tumor during air breathing (*Upper*) and carbogen breathing (*Lower*). The expanded tumor region, given at *Right*, clearly shows heterogeneity in pO_2 distribution.

>20 even at the low power. Using Eqs. **6** and **7**, the concentration of Oxo63 and the pO_2 maps were obtained. It was found that when the SNR of the low power image was >20, the uncertainty in voxel pO_2 was ±10%.

Fig. 3 shows Oxo63 and O_2 concentration maps of a mouse infused with a bolus of Oxo63 (3.8 mmol/kg). As in the case of the intensities in the anatomic images (Figs. 1 and 2), the concentration of Oxo63 was found to be higher in kidney and in tumors. However, the pO_2 images show interesting differences compared with the Oxo63 images, especially in tumors. Oxo63 concentrations were found to vary between 0.4 and 2 mM across the tumor, indicating differences in perfusion; the pO_2 images suggest that this tumor (SCC), even at 1 cm diameter, is significantly hypoxic (>85% pixels with <10 mmHg).

The oxygenation status of cancer cells is known to affect the outcome of radiotherapy, with oxygenated cells being more radiosensitive than hypoxic cells. Increasing the oxygen available to the cells can be accomplished by inhaling high-oxygen gas mixtures such as carbogen (26). To test the dynamic nature of the OMRI experiment, oxygen mapping in tumor-bearing mice was carried out by altering the oxygen concentration in the inspired gas. Fig. 4 shows images of pO_2 distribution in an SCC tumor-bearing mouse during air (*Upper*) and carbogen (*Lower*) breathing. Shown in Fig. 4 *Right* is an enlarged presentation of the images from the tumor region. Similar to the results shown in Fig. 3, the results from this experiment suggest that spin probe Oxo63 localizes in the tumor effectively and reports on the oxygen status. Although the oxygen status in the tumor reveals severely hypoxic regions, increase in the pO_2 status in response to carbogen breathing was observed.

Monitoring pO_2 by using Eppendorf electrodes is a well-established technique for *in vivo* studies (6). To examine the quantitative tumor pO_2 imaging capabilities of OMRI, the pixel tumor pO_2 values obtained from the parametric OMRI images of mice breathing air or carbogen were plotted as frequency histograms and compared with the corresponding pO_2 histograms constructed from Eppendorf electrode measurements. The age of the mice, tumor type and size, and anethestetics used were maintained constant. Fig. 5 shows these pO_2 histograms. The mean pO_2 values obtained by using OMRI from mice breathing air were 0.5 ± 1.4 mmHg ($n = 5$) and 18.8 ± 1.33 mmHg ($n = 5$) when breathing carbogen. The corresponding measurements using Eppendorf electrode were 1.4 ± 0.1 mmHg for mice breathing air ($n = 14$) and 15.8 ± 1.8 mmHg ($n = 7$) when breathing carbogen. The error limits were based on the variance from all of the measurements from all of the animals. As can be seen, the agreement in pO_2 obtained with the "gold standard" Eppendorf electrode validates the quantitative pO_2 imaging capabilities of OMRI. There was no statistical difference in the pO_2 values obtained by OMRI and Eppendorf electrode when the mice were breathing air ($P = 0.6$) or carbogen ($P = 0.2$), further validating the quantitative pO_2 imaging capabilities of

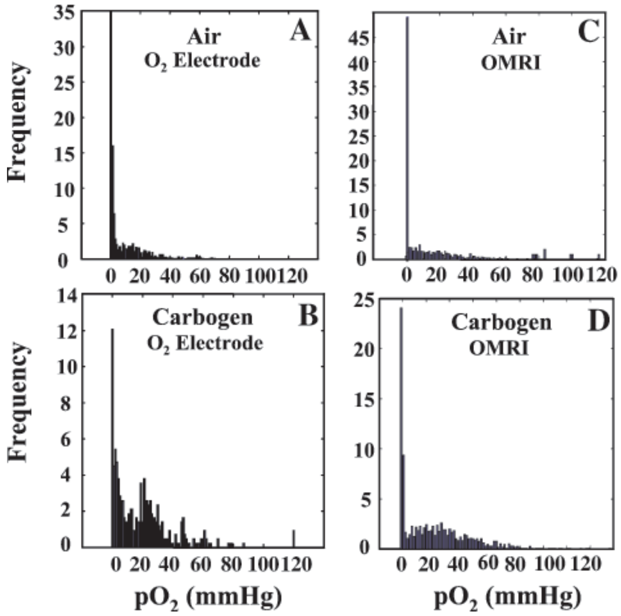

Fig. 5. Comparison of pO_2 histograms of tumor oxygen distribution computed from OMRI images, and independently obtained from oxygen electrode measurements for air and carbogen breathing.

OMRI. Although >58% of the tumor regions reported pO_2 values of <5 mmHg when the animal was breathing air, <35% of the tumor reported <5 mmHg on carbogen inhalation.

Discussion

The presence of tumor hypoxia has long been identified as a potential limitation to the effectiveness of radiation therapy; however, there have been relatively few options to assess tissue oxygen concentrations noninvasively. Likewise, the ability to measure oxygen concentrations in cardiac and brain tissues would have widespread applications in patient management. The results of this study clearly indicate that OMRI yields physiologic information in addition to high-resolution anatomical detail during a single examination and holds promise for characterizing tissue oxygenation (at least for tumor tissue). Further, the study confirms the feasibility of measuring tissue pO_2 with reasonable accuracy, sensitivity, and repeatability needed for clinical utility. The pO_2 images of the tumor (Fig. 4) show distinct intratumor heterogeneity with a gradation of oxygen concentration. The pO_2 values range from hypoxic to normoxic values (≈50 mmHg) and are comparable with tumor pO_2 values reported in using different invasive methods. The imaging times ranged between 4 and 8 min, and degradation of pO_2 maps caused by animal motion, system instability, and the contrast agent distribution were not observed during this period. This study also shows that OMRI is capable of monitoring changes in tumor oxygenation on alteration of the breathing gas. In general, mean pO_2 values increased on carbogen breathing. In particular, the percentage of extremely hypoxic regions (<5 mmHg pO_2) decreased ≈30% during carbogen breathing.

There are two important considerations relevant to the development of this methodology for clinical applications. These considerations are the signal intensity and the RF power deposition; these are interrelated, and one may be preferred over the other for optimal performance. The signal intensity determines the quality of the images and consequently the spatial resolution and accuracy of pO_2 values. Our experimental data show that an SNR above 10 (in the low power) gives a reliable estimate of pO_2 values with a 5-mmHg standard deviation at the lowest pO_2 level. The SNR values of the images given in Fig. 2 are 20 and 32 for low and high power, respectively. These images were obtained with a dose of 3.8 mmol/kg Oxo63, which is well within the LD_{50} values of Oxo63 for mouse. Improvements in instrumentation and contrast agents can enhance the SNR and consequently bring down the dose further. A crucial aspect of this method concerning its applicability to human studies is the power deposition caused by the EPR B_1 field, which may cause undesired heating especially above 300 MHz. The RF coil used for EPR irradiation can be modified to decrease the power deposition. At present, a saddle coil is used for EPR irradiation. The use of a quadrature coil would enhance the SNR by a factor of 1.4 for the same power or permit reduction of the EPR power by 3 dB for the same SNR to avoid RF heating (27). Pulsed EPR irradiation by a train of alternating pulses has been suggested to bring down the average EPR power (28). Topical resonators that provide good homogeneity and sensitivity in a defined volume of interest may also be used to enhance the SNR, as well as to reduce the total power deposited in the body. The multiring surface coil may be particularly appropriate for functional imaging studies of a defined volume of interest (29). Additionally, developing new spin probes with narrower line widths, compared with those currently used, will help in decreasing the RF power deposition. A few other trityl radicals are reported to have narrower resonance than Oxo63 (20). These agents may show better enhancement than Oxo63. For example, the average power level for half saturation of the fully deuterated Oxo63 is 3 dB (50%) less than Oxo63. With future developments and refinements, OMRI may become viable functional imaging modality for clinical applications.

Conclusions

This work demonstrates the feasibility of generating MR images with both morphological and functional information at 0.015 T. The OMRI-based noninvasive approach can be used to continuously assess tumor oxygenation status at specific locations within a tumor. The pO_2 maps obtained from tumor are quantifiable and reproducible, and correlate well with the Eppendorf measurements. The *in vivo* animal images, generated by using the prototype scanner system, demonstrate superior SNR and resolution compared with other studies. Many physical and chemical means for improving the sensitivity of this method do exist. With these improvements, this noninvasive technique could be further developed as a tool to assess changes in tumor oxygenation, to evaluate the pharmacological effect of anti-neoplastic drugs, and as a prognostic indicator of therapeutic response.

We sincerely thank Prof. A. W. Overhauser and the reviewers of this manuscript for valuable suggestions, and the technical help of the staff of Philips Research Laboratory, Hamburg, Germany.

1. Horsman, M. R., Nordsmark, M. & Overgaard, J. (1998) *Strahlenther. Onkol.* **174,** 2–5.
2. Stratford, I. J., Adams, G. E., Bremner, J. C., Cole, S., Edwards, H. S., Robertson, N. & Wood, P. J. (1994) *Int. J. Radiat. Biol.* **65,** 85–94.
3. Maxwell, P. H., Dachs, G. U., Gleadle, J. M., Nicholls, L. G., Harris, A. L., Stratford, I. J., Hankinson, O., Pugh, C. W. & Ratcliffe, P. J. (1997) *Proc. Natl. Acad. Sci. USA* **94,** 8104–8109.
4. Hockel, M., Schlenger, K., Aral, B., Mitze, M., Schaffer, U. & Vaupel, P. (1996) *Cancer Res.* **56,** 4509–4515.
5. Giaccia, A. J. (1996) *Semin. Radiat. Oncol.* **6,** 46–58.
6. Vaupel, P., Schlenger, K., Knoop, C. & Hockel, M. (1991) *Cancer Res.* **51,** 3316–3322.
7. Grucker, D. (2000) *Prog. Nucl. Magn. Reson. Spectrosc.* **36,** 241–270.
8. Krishna, M. C., Subramanian, S., Kuppusamy, P. & Mitchell, J. B. (2001) *Semin. Radiat. Oncol.* **11,** 58–69.
9. Subczynski, W. K., Lukiewicz, S. & Hyde, J. S. (1986) *Magn. Reson. Med.* **3,** 747–754.
10. Mazurchuk, R., Zhou, R., Straubinger, R. M., Chau, R. I. & Grossman, Z. (1999) *Magn. Reson. Imaging* **17,** 537–548.
11. Halpern, H. J., Yu, C., Peric, M., Barth, E., Grdina, D. J. & Teicher, B. A. (1994) *Proc. Natl. Acad. Sci. USA* **91,** 13047–13051.
12. Velan, S. S., Spencer, R. G., Zweier, J. L. & Kuppusamy, P. (2000) *Magn. Reson. Med.* **43,** 804–809.
13. Hunjan, S., Mason, R. P., Constantinescu, A., Peschke, P., Hahn, E. W. & Antich, P. P. (1998) *Int. J. Radiat. Oncol. Biol. Phys.* **41,** 161–171.
14. Jue, T. & Anderson, S. (1990) *Magn. Reson. Med.* **13,** 524–528.
15. Pratt, R. G., Zheng, J., Stewart, B. K., Shiferaw, Y., McGoron, A. J., Samaratunga, R. C. & Thomas, S. R. (1997) *Magn. Reson. Med.* **37,** 307–313.
16. Guiberteau, T. & Grucker, D. (1997) *J. Magn. Reson.* **124,** 263–266.
17. Lurie, D. J., Bussell, D. M., Bell, L. H. & Mallard, J. R. (1988) *J. Magn. Reson.* **76,** 366–370.
18. Overhauser, A. W. (1953) *Phys. Rev.* **92,** 411–412.
19. Golman, K., Petersson, J. S., Ardenkjaer-Larsen, J. H., Leunbach, I., Wistrand, L. G., Ehnholm, G. & Liu, K. (2000) *J. Magn. Reson. Imaging* **12,** 929–938.
20. Ardenkjaer-Larsen, J. H., Laursen, I., Leunbach, I., Ehnholm, G., Wistrand, L. G., Petersson, J. S. & Golman, K. (1998) *J. Magn. Reson.* **133,** 1–12.
21. Roques, B. P., Rao, R. & Marion, D. (1980) *Biochimie* **62,** 753–773.
22. Griffey, R. H. & Redfield, A. G. (1987) *Q. Rev. Biophys.* **19,** 51–82.
23. Lee, J. N. (1996) *J. Magn. Reson. Imaging.* **1,** 261–263.
24. Grucker, D., Guiberteau, T. & Eclancher, B. (1995) *Magn. Reson. Med.* **34,** 219–226.
25. Golman, K., Leunbach, I., Ardenkjaer-Larsen, J. H., Ehnholm, G. J., Wistrand, L. G., Petersson, J. S., Jarvi, A. & Vahasalo, S. (1998) *Acta Radiol.* **39,** 10–17.
26. Robinson, S. P., Rodrigues, L. M., Ojugo, A. S., McSheehy, P. M., Howe, F. A. & Griffiths, J. R. (1997) *Br. J. Cancer.* **75,** 1000–1006.
27. Glover, G. H., Hayes, C. E., Pelc, N. J., Edelstein, W. A., Mueller, O. M., Hart, H. R., Hardy, C. J., O'Donnell, M. & Barber, W. D. (1985) *J. Magn. Reson.* **64,** 255–270.
28. Alecci, M. & Lurie, D. J. (1999) *J. Magn. Reson.* **138,** 313–319.
29. King, S. B., Ryner, L. N., Tomanek, B., Sharp, J. C. & Smith, I. C. (1999) *Magn. Reson. Med.* **42,** 655–664.